J Nanopart Res (2015) 17:451
DOI 10.1007/s11051-015-3251-7

RESEARCH PAPER

Synthesis, optical properties and photodegradation for methylene blue of Ni-vanadate $K_2Ni(VO_3)_4$ nanoparticles

Yuting Lu · Yinfu Pu · Yanlin Huang · Jing Wang · Juan Lu

Received: 3 May 2015 / Accepted: 7 November 2015 / Published online: 23 November 2015

Abstract A Ni^{2+}-containing vanadate, $K_2Ni(VO_3)_4$ was developed as a new visible-light-driven photocatalyst. The nanoparticles were prepared by the modified Pechini method. The sample was characterized by the measurements such as X-ray powder diffraction, scanning electron microscope, and UV–Vis absorption spectrum. The photocatalytic activity of $K_2Ni(VO_3)_4$ nanoparticles was evaluated by the photodegradation of methylene blue under visible-light irradiation in air. $K_2Ni(VO_3)_4$ shows a photocatalytic activity due to the efficient absorption in the UV–Visible-light wavelength region with a narrowed band-gap energy of 2.08 eV and an indirectly allowed electronic transition. These results indicate that this vanadate garnet could be a potential photocatalyst driven by visible light. The effective photocatalytic activity was discussed on the basis of the special structural characteristic such as heavily distorted NiO_6, rich, activated optical centers with tunnel structure for high photocatalytic capacity, and discussed on the basis of the photoluminescence and the decay lifetime.

Keywords Semiconductors · Catalysis · Electronic band structure · Optical absorption and reflection · Luminescence

Introduction

Semiconductors have been intensively investigated as efficient photocatalysts to oxidize organic pollutants into nontoxic products or deplete H_2O (Karahaliloglu et al. 2014; Kandula and Jeevanandam 2014; Nogueira et al. 2014; Ramadan et al. 2013; Weng et al. 2014). Until now, semiconductors have been developed to be potential photocatalysts such as TiO_2 (Zhang et al. 2015; Zhu et al. 2014; Liu et al. 2015; Lázaro-Navas et al. 2015), ZnO (Yin et al. 2014), Bi_2O_3 (Dang et al. 2015), CdS (Xiong et al. 2015), $NaTaO_3$ (Su et al. 2015), Bi_2WO_6 (Song et al. 2015), $SrTiO_3$ (Márquez-Herrera et al. 2014), Fe_3O_4 (Zhang et al. 2014a, b), Co_3O_4 (Elazab et al. 2014), etc. Among them, TiO_2 is certainly the most widely investigated photocatalyst for its high efficiency, nontoxic nature, photochemical stability, and low cost.

Usually, the oxides such as TiO_2 has a large band gap (3.2 eV) (Lu et al. 2014; Chadha et al. 2014), and therefore, only UV light can be absorbed. This limits its application in the industrial field because the UV light accounts for merely 5 % of the sunlight energy. It is necessary that the band gap of a material is narrow enough between 1.9 and 3.1 eV with an optimal value of 2.03 eV to harvest visible light (400 nm $< \lambda <$ 760 nm)

Y. Lu · Y. Pu · Y. Huang (✉) · J. Wang · J. Lu (✉)
College of Chemistry, Chemical Engineering and Materials Science, Soochow University, Suzhou 215123, China
e-mail: huang@suda.edu.cn

J. Lu
e-mail: lujuan@suda.edu.cn;
juanlu@suda.edu.cn

which accounts for ~45 % of the solar spectrum's energy (Murphy et al. 2006). In order to reach this goal, the photocatalytic properties have been obtained by many methods in the different modifications such as Gold-nanocage-coupled TiO_2 (Chadha et al. 2014), g-C_3N_4-P25/TiO_2 (Zhu et al. 2014), La/N-codoped TiO_2 (Liu et al. 2015), Pt@SiO_2@TiO_2 (Zhang et al. 2015), and NiO/N-doped TiO_2 (Li et al. 2015). It is well known that to extend the activity of a photoelectrode into the visible-light region, various new methods of photocatalysts have been investigated.

In this work, we try to develop a new photocatalyst, Ni-containing vanadate $K_2Ni(VO_3)_4$. The research motivations are the followings. First, one of the most characteristic features is that the band-gap energy of the photocatalyst can be narrowed. Usually, Ni-3d energy band plays an important role in deciding the visible-light-induced photocatalytic activity (Yao and Ye 2006). For example, Wang et al. (2005) have reported that in $M_3V_2O_8$ (M = Mg, Ni, Zn) with the same structure, $Ni_3V_2O_8$ presents a smaller band gap of 2.25 eV than those of $Mg_3V_2O_8$ (3.02 eV) and $Zn_3V_2O_8$ (2.92 eV). This is induced by the split Ni-3d orbitals inserted between the O-2p and the V-3d orbitals in $Ni_3V_2O_8$. It also has been confirmed that an occupied level was created in the center of the band gap due to the Ni-3d band splitting in the oxides such as Ni^{2+}-doped TiO_2 and $SrTiO_3$ (Kudo et al. 2007). The results show that the Ni^{2+} addition shows an efficient photocatalytic performance and an excellent photo stability in photocatalytic materials such as Ni-laded TiO_2 (Liu et al. 2014), $Ni_xCd_{1-x}S$ (Chen et al. 2015), Ni-doped $InVO_4$ (Zhang 2014), and NiO/N-doped TiO_2 (Li et al. 2015).

Second, $K_2M(VO_3)_4$ (M = Ni^{2+}, Zn^{2+}, Mn^{2+}) has monoclinic structure constructed by a metal–oxygen polyhedral framework. Figure 1a is an example structural view of the unit cell of $K_2Ni(VO_3)_4$ along [100] direction obtained from the inorganic crystal structure database (Witzke et al. 2001; Liao et al. 1996). The metal V^{5+} ions (in $[VO_4]^{3-}$) completely occupy the fourfold T_d sites. The V–O distances are changed from 1.645 to 1.781 Å. There is an infinite VO_4 chain along [100] in the lattices as shown in Fig. 1b. The Ni^{2+} ions are located in the NiO_6 octahedral sites in a tunnel along [100] displayed in Fig. 1c. The Ni–O band length ranges from 2.0683 to 2.1266 Å. There are two kinds of optically active centers in the lattices, i.e., NiO_6 and VO_4. Under light excitation, photoinduced electrons can be easily created from O-2p to the empty Ni-3d, or by the charge transfer (CT) of an electron from the oxygen 2p orbital to the vacant 3d orbital of V^{5+} (Nakajima et al. 2009). The separated excitons could react with dye molecules into nontoxic products.

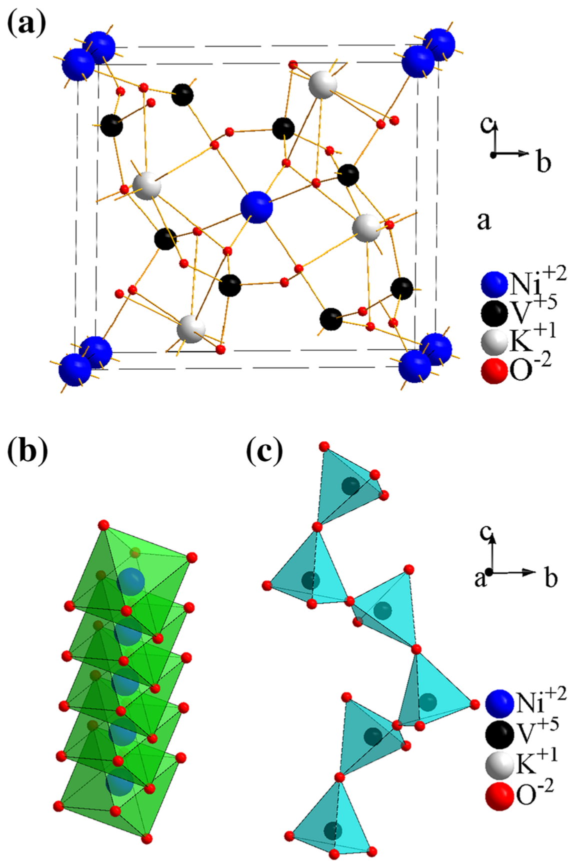

Fig. 1 Schematic structure views of $K_2Ni(VO_3)_4$ nanoparticles along [100] direction

$K_2Ni(VO_3)_4$ nanoparticle powders were developed by the modified Pechini method. The sample was investigated by the crystal phase, morphologies, UV–Vis absorption, and band-gap structure. The efficient photocatalytic activity was confirmed by the degradation of methylene blue (MB) under visible-light irradiation, which was discussed on the base of the crystal structure.

Experimental

$K_2Ni(VO_3)_4$ nanoparticles were prepared by the Pechini method. The raw materials are stoichiometric amounts of potassium nitrate (KNO_3), nickel nitrate ($Ni(NO_3)_2 \cdot 6H_2O$) and ammonium meta-vanadate (NH_4VO_3). As an example, the raw materials of 1.01 g KNO_3, 1.49 g $Ni(NO_3)_2 \cdot 6H_2O$, 2.34 g NH_4VO_3 were first dissolved in deionized water. The nitrate solutions were complexed by citric acid with the double molar weight of the cations. The three solutions were mixed uniformly, and the mixed solution was neutralized by controlled addition of ammonium hydroxide (30 wt%). The solution was promoted by heat treatment at 80–95 °C for 1–3 h. Then, a certain amount of aqueous polyvinylalcohol (PVA) was slowly added in the solution to adjust the viscoelasticity of the solution. The mixed solution was stirred for 1–3 h to obtain a homogeneous viscous solution for the spin-coating on several clean glasses. The dried precursor thin film can be obtained by natural withering of the coated glasses. Then, the films were taken down from the glasses, and then heated at 680 °C in a muffle furnace. Finally, $K_2Ni(VO_3)_4$ nanopowders can be obtained. Another isostructural sample of $K_2Zn(VO_3)_4$ was also prepared in the same method to make a comparison of optical absorption and photocatalysis. The referred sample also keeps a pure crystal phase and has similar morphology to those of $K_2Ni(VO_3)_4$ nanoparticles. The motivation is to elucidate the role of Ni^{2+} ions in the lattices which can narrow the band gap and promote the photocatalysis under near-UV light.

XRD was obtained using a Rigaku D/Max diffractometer operating at 40 kV, 30 mA with Cu Kα as an incident radiation. The SEMs were used to study the surface morphologies of the samples. Diffuse reflection spectra (DRS) were taken on a Cary 5000 UV–Vis–NIR spectrophotometer by means of $BaSO_4$ powder as a standard reference. X-ray photoelectron spectroscopy (XPS) analyses were performed using an XPS, Kratos analytical, ESCA-3400, Shimadzu. Nitrogen adsorption and desorption isotherms were obtained on an ASAP 3020 (Micromeritics Instruments, USA), a nitrogen adsorption apparatus. All the samples were degassed at 150 °C to remove the absorbed gases prior to the nitrogen adsorption measurement. Particle sizes and size distributions of the particles were measured using a particle size analyzer (Mastersizer 3000, Malvern, UK) by dynamic light scattering (DLS) technique. The specific surface area (S_{BET}) was determined by a multipoint BET method using the adsorption data in the relative pressure (P/P_0) range of 0.05–0.3. The adsorption isotherm data were used to determine the pore-size distribution via the Barret–Joyner–Halender (BJH) method, assuming a cylindrical pore model. The adsorbed nitrogen volume at the relative pressure (P/P_0) of 0.99 was used to determine the pore volume and the average pore size.

Photocatalysis experiments were carried out in a quartz beaker filled with MB solution (100 mL and 10–40 mg/L) containing the catalyst (0.25 g/L). A 300-W Xenon lamp with a UV cutoff filter (JB450) was positioned at about 10 cm beside the photoreactor. Prior to visible-light irradiation, the suspension was dispersed by ultrasonic irradiation for 40 min in dark to favor the adsorption and desorption equilibration. The concentration of MB was analyzed by recording the absorption band maximum (665 nm) in the absorption spectra and taken as the initial concentration (C_0). During the photocatalysis, 7 mL of the suspension was extracted at an interval of 10 min, and the absorption (C) was measured after 5 min of centrifugation. The normalized temporal concentration changes (C/C_0) of MB were obtained.

Results and discussions

Phase formation and surface structure

The crystal phase of $K_2Ni(VO_3)_4$ nanoparticles was investigated by XRD measurement as shown in Fig. 2. The pattern is in agreement with the standard card PDF#44-0350 in the International Centre for Diffraction Data (ICDD) database. All the diffraction peaks in XRD pattern can be well indexed on the basis of the monoclinic structure of $K_2Ni(VO_3)_4$. No impurity lines can be observed.

The typical scanning electron microscopy (SEM) images of $K_2Ni(VO_3)_4$ nanoparticles in two magnifications are shown in Fig. 3a, b. The sample crystallized in the irregular ball-like nanoparticles. The size distribution of the nanoparticles was determined by dynamic light scattering (DLS) technique as shown in Fig. 3c. The average size of the nanoparticles estimated by the micrograph is 67 nm. TEM image of $K_2Ni(VO_3)_4$ nanoparticles is shown in Fig. 3d. It confirms that $K_2Ni(VO_3)_4$ nanoparticles are well crystallized with a single-phase structure, which is in good agreement with the observed XRD pattern. The

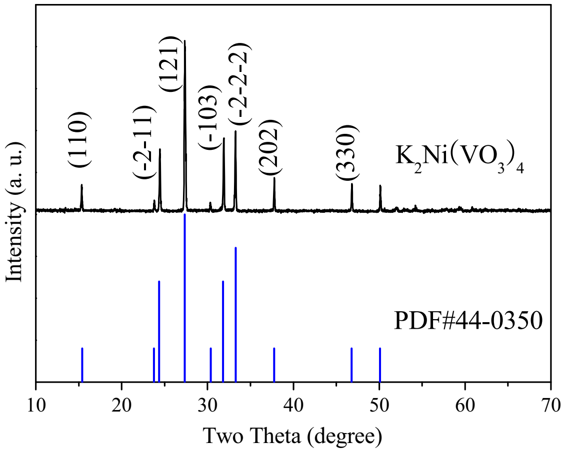

Fig. 2 The experimental X-ray diffraction profiles of $K_2Ni(VO_3)_4$ nanoparticles

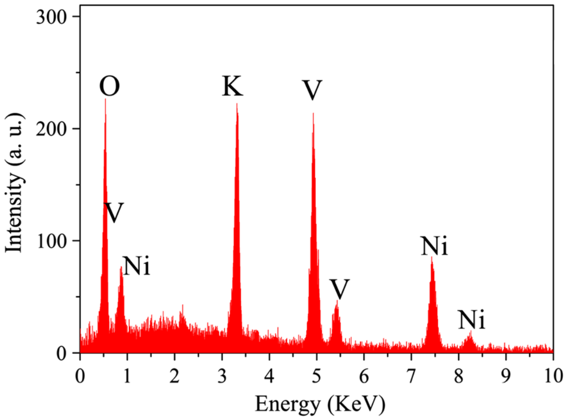

Fig. 4 The EDS spectrum of $K_2Ni(VO_3)_4$ nanoparticles

Fig. 3 The typical SEMs (**a**, **b**), the size distributions (**c**), and the TEM images (**d**) of $K_2Ni(VO_3)_4$ nanoparticles

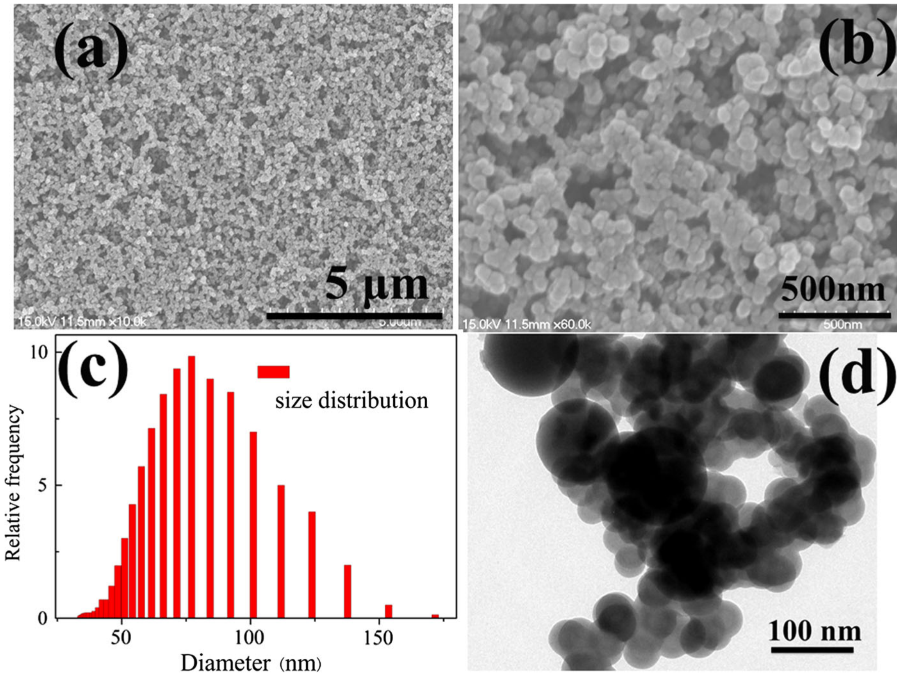

particles reveal the formation of spherical grains of nanonature (size <100 nm), which presents some aggregations. Figure 4 shows the EDS measurement to examine the elemental compositions on the sample. Several specific lines show the signals of Ni, K, V, and O elements. The average Ni/V ratio was calculated to be about 0.234, which is in agreement with the theoretical stoichiometric value in the chemical formulae of $K_2Ni(VO_3)_4$.

BET surface area and pore-size distribution

BET surface area and pore-size distribution of the nanoparticles were investigated. Figure 5 shows the N_2 adsorption–desorption isotherm and the corresponding pore-size distribution curve of $K_2Ni(VO_3)_4$. According to the IUPAC classification, the isotherm of the sample is of the typical IV pattern, which is characterized with a hysteresis loop. The high

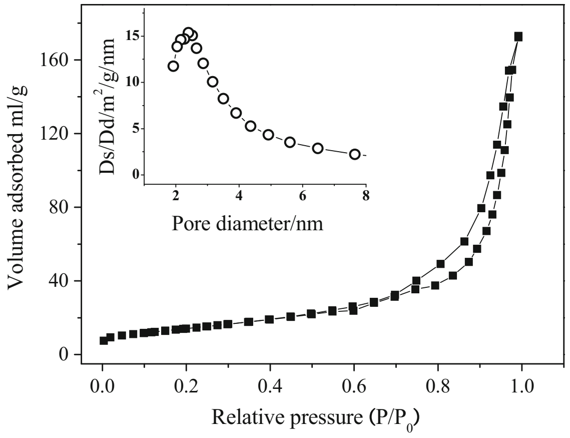

Fig. 5 The nitrogen adsorption–desorption isotherms of $K_2Ni(VO_3)_4$ nanoparticles; *inset*: the corresponding pore-size distribution curve

adsorption at P/P_0 approaching to 1.0 indicates the coexistence of mesopores and macropores. The specific surface area of $K_2Ni(VO_3)_4$ particles was measured to be 56 m^2 g^{-1}. The pore-size distribution of the sample was quite narrow and monomodal, implying that the prepared nanoparticles are uniform. The pore-size distribution is centered on 3 nm (inset Fig. 5).

Optical absorption and band-gap structure

The UV–Vis absorption spectrum of $K_2Ni(VO_3)_4$ nanoparticles is shown in Fig. 6a. There is a very broad optical transition from 200 to 600 nm. The onset wavelength around 600 nm corresponds to an optical band gap if a single transition was assumed. The absorption band can be divided into three distinct absorption bands, i.e., I: 200–400 nm, II: 400–600 nm, and III: 600–800 nm.

Absorption III can be unambiguously assigned to the spin-allowed *d–d* transitions from the Ni^{2+} ions in the octahedral environment, i.e., $^3A_{2g}(F) \rightarrow {}^3T_{1g}(F)$ (Biswas et al. 2008). While bands I and II form the band-gap transitions, i.e., one is from CT transitions inside VO_4^{3-} groups, and another is the spin-allowed *d–d* transitions from the Ni(II) ions in the octahedral environment of $^3A_{2g}(F) \rightarrow {}^3T_{1g}(P)$ (Biswas et al. 2008), respectively.

CT band edge in VO_4^{3-} groups has been reported only in UV to near-UV wavelength region, not extending to blue region (Nakajima et al. 2009). Consequently, the absorption in UV region I: 200-400 nm can be assigned to the CT ($O^{2-} \rightarrow V^{5+}$) in VO_4^{3-} groups. This can be clearly understood by the comparison of the optical absorption of $K_2Zn(VO_3)_4$ in Fig. 6a, which have no optical-activated cations in K and Zn ions. By the way, the absorption band II corresponds to the spin-allowed d–d transitions of the Ni^{2+} in octahedral in $K_2Ni(VO_3)_4$. Such a typical absorption has been reported in Ni-containing photocatalysts such as $Ni_3V_2O_8$ (Wang et al. 2005) and $CsLaSrNb_2NiO_9$ (Yao and Ye 2006).

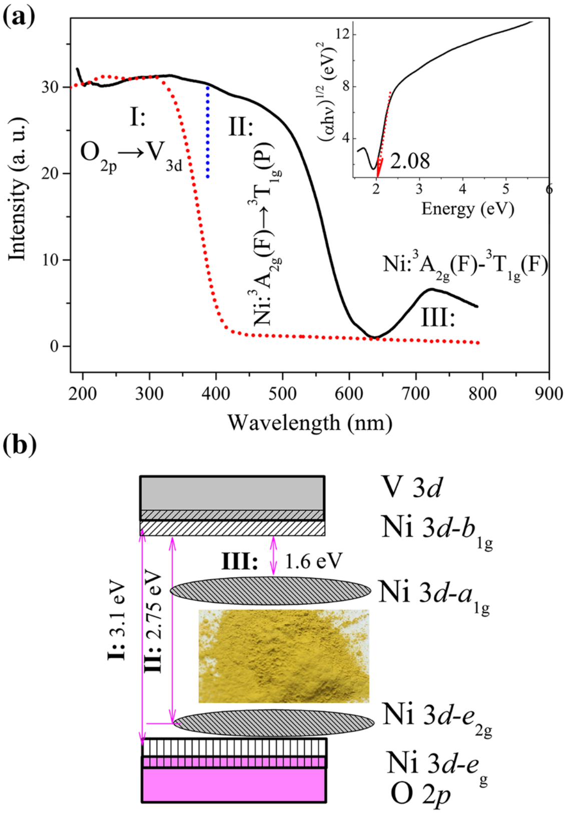

Fig. 6 **a** UV–Vis absorption spectrum of $K_2Ni(VO_3)_4$ compared with $K_2Zn(VO_3)_4$, *inset* showing the estimated band gap, and the band-gap structure; **b** the schematic band-gap structure, *inset* showing the digital photo of the powders

Figure 6b shows the schematic band structure of $K_2Ni(VO_3)_4$, with reference to the reported results in Ni^{2+}-containing oxides. The absorption bands I and II form the band-gap components with the valence band (VB) of (Ni 3d + O 2p) to the conduction band (CB) of (V 3d + Ni 3d-b_{1g}). For Ni^{2+} with the electronic configurations $3d^8$ in the photocatalysts, the split Ni 3d-t_{2g} orbitals were fully occupied, while the split Ni 2d-e_g orbitals should be partially occupied. Yao and Ye (2006) have suggested that Ni 2d-e_g orbitals can further split into two parts for the distortion of the Ni–O octahedrons (Yao and Ye 2006), and the lower energy band a_{1g} orbitals were assumed to be fully occupied to have better consistency with the photophysical and photocatalytic properties of the photocatalysts as shown in Fig. 6b. The absorption band II: 2.75 eV and band III: 1.6 eV were assumed to form Ni 3d-b2 g and Ni 3d-a1 g orbitals, respectively, by the further splitting of Ni 3d orbitals in the octahedral field. As shown in inset Fig. 6a, $K_2Ni(VO_3)_4$ particles are deep yellow. The color should be generally attributed to crystal-field transitions along with some contributions from the allowed d–d transitions of the Ni^{2+} in octahedral environment.

The band-gap energy E_g was determined by the Wood-Tauc theory based on the relation of $\alpha h\upsilon \propto \left(h\upsilon - E_g\right)^k$, where α is the absorbance, h is the Planck constant, v is the frequency, and k is a constant associated to the different types of electronic transitions ($k = 1/2$, 2, 3/2, or 3 for directly allowed, indirectly allowed, directly forbidden, or indirectly forbidden transitions, respectively). The best linear relation of $K_2Ni(VO_3)_4$ nanoparticles was obtained for k value of 2 shown in inset Fig. 6a, indicating this is an indirectly allowed electronic transition. The band gap of $K_2Ni(VO_3)_4$ particles is calculated to be about 2.08 eV, which is significantly narrower than the reported vanadates such as $Ni_3V_2O_8$ (2.25 eV) and $Zn_3V_2O_8$ (2.92 eV) (Wang et al. 2005). This also demonstrates that the substitution of Ni^{2+} can significantly reduce the band gap of a compound, which is beneficial to the improvement of the photocatalytic activity.

Theoretically, the positions for valence band and conduction band are determined by the Eqs. (1) and (2) (Ohko et al. 1997; Butler and Ginley 1978):

$$E_{VB} = X - E^e + 0.5\,E_g \tag{1}$$

$$E_{CB} = X - E^e + 0.5\,E_g \tag{2}$$

E_g is the energy of the band gap, X is the absolute electronegativity of the semiconductor (geometric mean of the absolute electronegativity of the constituent atoms). E^e is defined as the energy of free electrons on the hydrogen scale (~4.5 eV vs SHE). Here the experimental E_g is 2.08 eV for $K_2Ni(VO_3)_4$ nanoparticles. The corresponding CB and VB levels of $K_2Ni(VO_3)_4$ nanoparticles are calculated to be −0.002 and 2.078 eV versus SHE, respectively. The result shows that $K_2Ni(VO_3)_4$ nanoparticles is difficult for photocatalytic hydrogen generation.

XPS spectra

It is well known that V and Ni elements have multiple valences in compounds. Binding energy X-ray photoelectron spectroscopic (XPS) measurement can provide useful information on the oxidation states of different elements in the lattices of materials. Figure 7a displays the typical XPS survey spectra of $K_2Ni(VO_3)_4$ nanoparticles. It is observed that the XPS peaks corresponding to K, Ni, V and O were identified in the sample.

The Ni-$2p_{3/2}$ XPS spectrum (Fig. 7b) shows the characteristic satellite peak with the binding energy (BE) at 864.2 eV. Such a satellite peak has been reported in Ni-containing oxides such as NiO (Carley et al. 1999) and $LiNi_{0.5}Mn_{0.5}O_2$ (Manikandan et al. 2011). The reason for such satellite peak is explained as due to the multiple splitting in the energy levels of the Ni-oxides (Carley et al. 1999). The V-2p XPS curve of the $K_2Ni(VO_3)_4$ nanoparticles is presented in Fig. 7c. The V-$2P_{3/2}$ and V-$2P_{1/2}$ peaks of the spinel appear at 517.2 and 524.5 eV, respectively. The values were close to those for $LiVO_3$ (Kumagai et al. 1996) and $LiNiVO_4$ (Prakash et al. 2013). The dominated signal at 517.2 eV was confirmed from V^{5+} ions by V oxidation at the crystal surface in $K_2Ni(VO_3)_4$. The XPS curve of V 2p (Fig. 7d) shows a slight asymmetric profile. This could be related to the possible effects of defect oxygen and adsorbed oxygen on the surfaces. For example, Zhang et al. (2014a, b) have demonstrated that there are rich induced V_o (oxygen vacancy) defects in the surfaces of $BiVO_4$. Recently, Rossell et al. (2015) have reported the detailed existence of V_O in $BiVO_4$: the O-related vacancy defects are in the 5-nm deepness of the surface.

Photocatalytic activity

The photocatalytic activity of $K_2Ni(VO_3)_4$ nanoparticles prepared by the Pechini method was tested by the degradation of a MB solution. Figure 8 shows the changes in UV/vis absorption spectra of MB-$K_2Ni(VO_3)_4$ solution under visible-light irradiation. The intensity of the peak at 665 nm significantly decreased with the increasing irradiation time. This peak decreased after illumination, suggesting that the

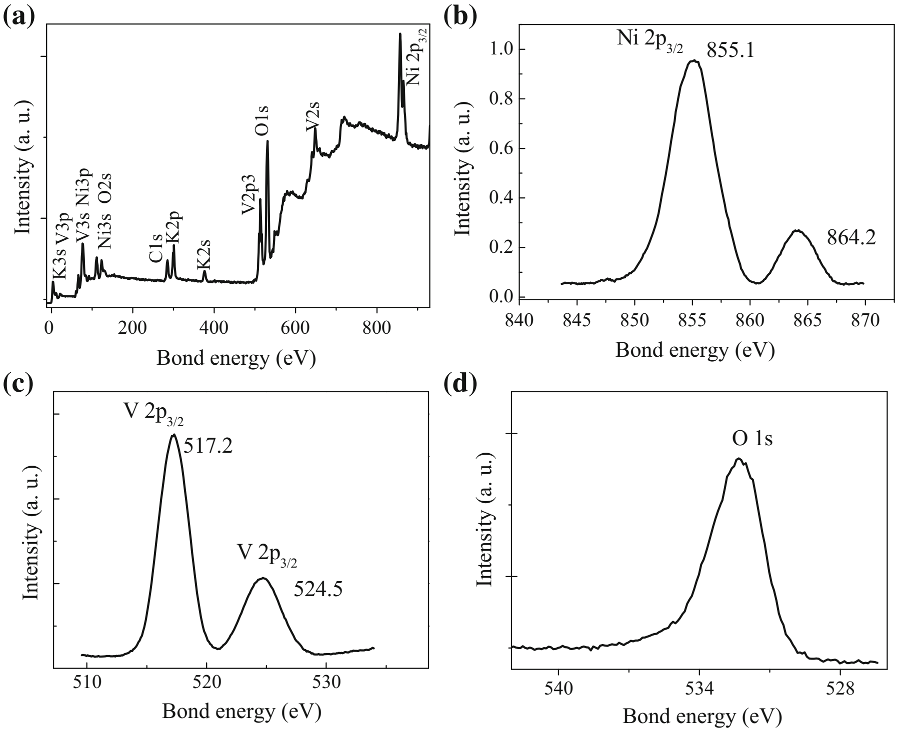

Fig. 7 The typical XPS survey spectra (**a**), and the XPS high-resolution spectra of Ni 2p (**b**), V 2p (**c**), and O 1 s (**d**) measured in $K_2Ni(VO_3)_4$ nanoparticles

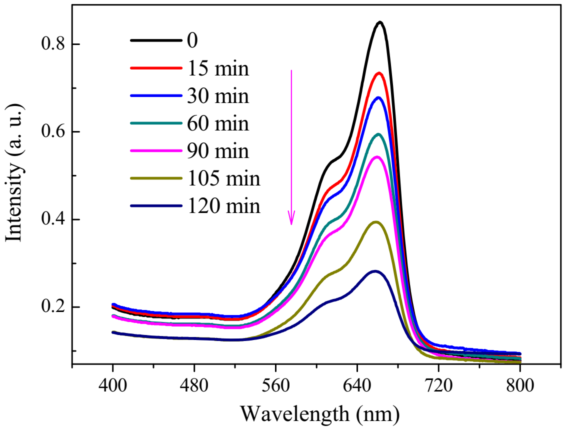

Fig. 8 The changes in UV–Vis absorption spectra of MB-$K_2Ni(VO_3)_4$ solution under visible-light irradiation

solution had been decolorized. Besides, the spectra keep the same profiles indicating that there were no new intermediates in the degradation process.

Figure 9 shows the photocatalytic degradation curve of MB by $K_2Ni(VO_3)_4$ nanoparticles compared with references of P25 photocatalyst and $K_2Zn(VO_3)_4$ under the same test condition; The inset is the degradation kinetics curve by means of plotting $\ln(C_0/C)$ versus irradiation time. The reference of $K_2Zn(VO_3)_4$ shows a small quantity of dye degraded under visible-light irradiation. The MB degradation rate of P25 is less than 40 %. In contrast, the degradation of the MB shows a fast speed in the presence of $K_2Ni(VO_3)_4$, which decreases to 20 % in 2 h. Moreover, according to the raw materials and preparation processes, the costs of $K_2Ni(VO_3)_4$ obtained in this work are lower than that for TiO_2.

The kinetic constant is determined from the pseudo-first-order reaction rate equation of $\ln(C_0/C_t) = kt$, where C_0 is the initial concentration of MB, C_t is the concentration of MB at time t, and k is a kinetic constant. The inset in Fig. 9 shows the plot of $\ln(C_0/C_t)$ versus irradiation time. The good linear fit indicates that the kinetics of the degradation reaction is controlled dominantly by a pseudo-first-order reaction. The kinetic constant of MB degradation by $K_2Ni(VO_3)_4$ is calculated to be 2.05×10^{-2} min^{-1}.

It is a fact that the photoinduced electrons in the lattices have several possible fates; the first is a radiative

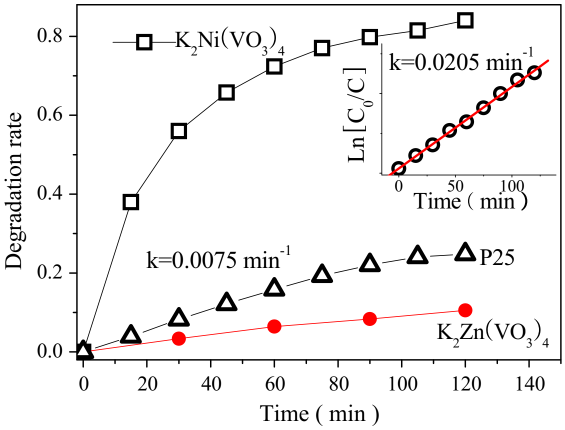

Fig. 9 Photocatalytic degradation curve of MB by $K_2Ni(VO_3)_4$ compared with references of P25 photocatalyst and $K_2Zn(VO_3)_4$ under the same test conditions. *Inset* shows the degradation kinetics by means of plotting $\ln(C_0/C)$ vs irradiation time

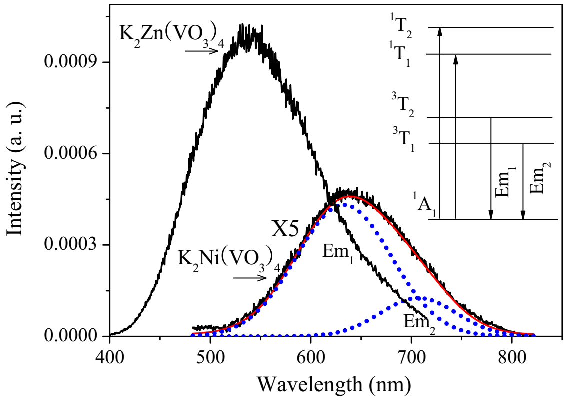

Fig. 10 Luminescence spectra of $K_2Ni(VO_3)_4$ excited by the excitation with 355-nm YAD:Nd laser. A reference emission of $K_2Zn(VO_3)_4$ was compared under the same test conditions. *Inset* shows the emission processes in VO_4 tetrahedron with T_d symmetry in vanadates

transition of recombination with a hole creating a luminescence in UV–Vis–IR wavelength region; the second one is nonradiative transition, which results in the heat generated by the transferring of energy to phonons in the lattices; the third one is the electrons, which could be trapped by any possible defects in the lattices; and the last one is the photoinduced electrons taking part in the photocatalytic process.

Vanadium, as a kind of efficient luminescent materials, has been developed in the previous years due to its various applications for lighting and display. The luminescence has been understood by the charge transfer (CT) transition in VO_4 with T_d symmetry (Nakajima et al. 2009). The molecular orbits of VO_4 are expressed as the ground $^1A_1$ state and excited $^1T_1$, $^1T_2$, $^3T_1$, and $^3T_2$ states (Fig. 10). The absorption transitions ($^1A_1 \rightarrow {}^1T_1, {}^1T_2$) are allowed ($Ex_1$, Ex_2), while the luminescence process ($^3T_1, {}^3T_2 \rightarrow {}^1A_1$) is forbidden in the ideal T_d symmetry due to the spin-selection rule. If the structure of VO_4 in a host is distorted from the idealized tetrahedron, the ($^3T_2$ and $^3T_1$) → $^1A_1$ transitions are allowed by the spin–orbit interaction, leading to two emission bands, Em_1 and Em_2, respectively (seen in Fig. 10) (Nakajima et al. 2009). In the lattices of $K_2Ni(VO_3)_4$, the VO_4 tetrahedron is heavily distorted and deviated from ideal tetrahedron T_d symmetry (Fig. 1). The VO_4 is connected by the corner with each other forming a chain along [100]. Consequently, the absorption transitions ($^1A_1 \rightarrow {}^1T_1$, $^1T_2$) are allowed, while the luminescence process ($^3T_1$, $^3T_2 \rightarrow {}^1A_1$) should not be forbidden (Nakajima et al. 2009).

Actually there is a very weak luminescence in $K_2Ni(VO_3)_4$ under excitation with a UV lamp. As shown in Fig. 10, $K_2Ni(VO_3)_4$ excited at 355 nm had a broad emission bands with the maximum wavelength at 650 nm. It is generally acknowledged that the higher fluorescence intensity means more recombinations of electron–hole pairs and lower photocatalytic activities (Hoffmann et al. 1995). As shown in Fig. 10, $K_2Zn(VO_3)_4$ has the broad emission bands with the maximum wavelength at 535 nm attributed to the ligand–metal CT bands (2p orbital of oxygen ion → 3d orbital of vanadium ion) localized within the tetrahedrally coordinated $[VO_4]^{3-}$ group. Compared with $K_2Zn(VO_3)_4$, the emission spectrum of $K_2Ni(VO_3)_4$ (650 nm) shows a great red-shift. This is corresponding to the narrower band gap. It is evident that the luminescence intensity of $K_2Ni(VO_3)_4$ is much lower than that of $K_2Zn(VO_3)_4$ suggesting a much lower recombination rate of photogenerated charge carriers in $K_2Ni(VO_3)_4$. This indicates that Ni^{2+} component in the lattices can effectively inhibit the recombination of excited electrons and holes.

It is commonly accepted that structure-induced dipole moments in distorted metal–oxygen polyhedra in the tunnel structural compounds are beneficial for the separation of hole–electron pairs, enhancing photocatalytic activities (Lin et al. 2006). The lattice of $K_2Ni(VO_3)_4$ presents channel structure formed by distorted NiO_6 along [100] as shown in Fig. 1b. The infinite chain's corner shares NiO_6 octahedra. Such a tunnel structure possesses a spatially open construction, leading to higher momentary polarizing fields that can work as accelerators for electron–hole separation. In such a tunnel, the presence of dipole moments heavily distorted NiO_6 octahedra resulting in an efficient photoexcitation, charge separation, and migration. This could enable the photoexcited electron–hole effectively to delocalize, enhancing the photocatalytic activity. It can be understood that a light radiation creates electron–hole pairs, i.e., exciton, in $K_2Ni(VO_3)_4$. Actually it can be observed that there is no luminescence in $K_2Ni(VO_3)_4$ indicating the weak recombination of the excitons. This could be suggested as due to a long lifetime of the excitons and more chances for electron–hole separations, which further react with dye molecules to oxidize the dye pollutant into nontoxic products.

Conclusions

A new visible-light-driven photocatalyst, $K_2Ni(VO_3)_4$ nanoparticles, was first developed by the modified Pechini method. $K_2Ni(VO_3)_4$ has a narrowed band gap of 2.08 eV characterized by an indirectly allowed electronic transition. The methylene blue dye can be efficiently degraded under visible-light irradiation in the presence of $K_2Ni(VO_3)_4$ nanoparticles. The photocatalytic ability is related to the structural features such as the regular VO_4 tetrahedron, the activated optical centers of NiO_6 octahedra with NiO_6 tunnel structure. The luminescence quenching in $K_2Ni(VO_3)_4$ could provide a low opportunity for the recombination of electron–hole pairs in the lattices. Accordingly, $K_2Ni(VO_3)_4$ possesses the improved the photocatalytic activity. The obtained nanoparticles could be expected to have a potential application in environment protection technology.

Acknowledgments This work was supported by the Priority Academic Program Development of Jiangsu Higher Education Institutions (PAPD), China.

References

Biswas SK, Dhak D, Pathak A, Pramanik P (2008) Chemical synthesis of environment-friendly nanosized yellow titanate pigments. Mater Res Bull 43:665

Butler MA, Ginley DS (1978) Prediction of flat band potentials at semiconductor-electrolyte interfaces from atomic electronegativities. J Electrochem Soc 125:228

Carley AF, Jackson SD, O'Shea JN, Roberts MW (1999) The formation and characterisation of Ni^{3+}-an X-ray photoelectron spectroscopic investigation of potassium-doped Ni(110)–O. Surf Sci 440:868

Chadha TS, Park J, An WJ, Biswas P (2014) Gold nanocage coupled single crystal TiO_2 nanostructures for near-infrared water photolysis. J Nanopart Res 16:2696

Chen W, Duan GR, Liu TY, Jia ZM, Liu XH, Chen SM, Yang XJ (2015) Synthesis of homogeneous one-dimensional $Ni_xCd_{1-x}S$ nanorods with enhanced visible-light response by ethanediamine-assisted decomposition of complex precursors. J Mater Sci 50:3920

Dang XM, Zhang XF, Chen YT, Dong XL, Wang GW, MaC Zhang XX, Ma HC, Xue M (2015) Preparation of β-Bi_2O_3/g-C_3N_4 nanosheet p-n junction for enhanced photocatalytic ability under visible light illumination. J Nanopart Res 17:93

Elazab HA, Moussa S, Gupton BF, El-Shall MS (2014) Microwave-assisted synthesis of Pd nanoparticles supported on Fe_3O_4, Co_3O_4, and $Ni(OH)_2$ nanoplates and catalysis application for CO oxidation. J Nanopart Res 16:2477

Hoffmann MR, Martin ST, Choi W, Bahnemann DW (1995) Environmental applications of semiconductor photocatalysis. Chem Rev 95:69

Kandula S, Jeevanandam P (2014) Visible-light-induced photodegradation of methylene blue using ZnO/CdS heteronanostructures synthesized through a novel thermal decomposition approach. J Nanopart Res 16:2452

Karahaliloglu Z, Hacker C, Demirbilek M, Seide G, Denkbas EB, Gries T (2014) Photocatalytic performance of melt-electrospun polypropylene fabric decorated with TiO_2 nanoparticles. J Nanopart Res 16:2615

Kudo A, Niishiro R, Iwase A, Kato H (2007) Effects of doping of metal cations on morphology, activity, and visible light response of photocatalysts. Chem Phys 339:104

Kumagai N, Fujiwara T, Tanno K, Horiba T (1996) Physical and electrochemical characterization of quaternary Li-Mn-V-O spinel as positive materials for rechargeable lithium batteries. J Electrochem Soc 143:1007

Lázaro-Navas S, Prashar S, Fajardo M, Gómez-Ruiz S (2015) Visible light-driven photocatalytic degradation of the organic pollutant methylene blue with hybrid palladium–fluorine-doped titanium oxide nanoparticles. J Nanopart Res 17:94

Li HR, Zhou J, Zhang XB, Zhou K, Qu SX, Wang JX, Lu X, Weng J, Feng B (2015) Constructing stable NiO/N-doped TiO_2 nanotubes photocatalyst with enhanced visible-light photocatalytic activity. J Mater Sci 26:2571

Liao JH, Sigala C, Guyomard D, Piffard Y (1996) $K_2Mn_3(OH)_2(VO_4)_2$: a new two-dimensional potassium manganese(II) hydroxyvanadate. Acta Crystallogr Sect C 52:284

Lin XP, Huang FQ, Wang WD, Wang YM, Xia YJ, Shi JL (2006) Photocatalytic activities of $M_2Sb_2O_7$ (M = Ca, Sr) for degrading methyl orange. Appl Catal A 313:218

Liu YH, Wang ZL, Fan WB, Geng ZR, Feng LB (2014) Enhancement of the photocatalytic performance of Niloaded TiO_2 photocatalyst under sunlight. Ceram Inter 40:3887

Liu JF, Li HY, Zong LL, Li QY, Wang XD, Zhang M, Yang JJ (2015) Photocatalytic oxidation of propylene on La and N codoped TiO_2 nanoparticles. J Nanopart Res 17:114

Lu DZ, Fang PF, Liu Y, Liu Z, Liu XZ, Gao YP, Chen FT, Niu F (2014) A facile one-pot synthesis of gadolinium doped TiO_2-based nanosheets with efficient visible light-driven photocatalytic performance. J Nanopart Res 16:2636

Manikandan P, Ananth MV, Kumar TP, Raju M, Periasamy P, Manimaran K (2011) Solution combustion synthesis of layered $LiNi_{0.5}Mn_{0.5}O_2$ and its characterization as cathode material for lithium-ion cells. J Power Sources 196:10148

Márquez-Herrera A, Ovando-Medina VM, Castillo-Reyes BE, Meléndez-Lira M, Zapata-Torres M, Saldaña N (2014) A novel synthesis of $SrCO_3$–$SrTiO_3$ nanocomposites with high photocatalytic activity. J Nanopart Res 16:2804

Murphy AB, Barnes PRF, Randeniya LK, Plumb IC, Grey IE, Horne MD, Glasscock JA (2006) Efficiency of solar water splitting using semiconductor electrodes. Int J Hydrogen Energy 31:1999

Nakajima T, Isobe M, Tsuchiya T, Ueda Y, Kumagai T (2009) A revisit of photoluminescence property for vanadate oxides AVO3 (A:K, Rb and Cs) and M3V2O8 (M: Mg and Zn). J Lumin 129:1598

Nogueira AE, Lima ARF, Longo E, Leite ER, Camargo ER (2014) Structure and photocatalytic properties of Nb-doped $Bi_{12}TiO_{20}$ prepared by the oxidant peroxide method (OPM). J Nanopart Res 16:2653

Ohko Y, Hashimoto K, Fujishima A (1997) Kinetics of photocatalytic reactions under extremely low-intensity UV illumination on titanium dioxide thin films. J Phys Chem A 101:8057

Prakash D, Masuda Y, Sanjeeviraja C (2013) Synthesis and structure refinement studies of $LiNiVO_4$ electrode material for lithium rechargeable batteries. Ionics 19:17

Ramadan W, Shaikh PA, Ebrahim S, Ramadan A, Hannoyer B, Jouen S, Sauvage X, Ogale S (2013) Highly efficient photocatalysis by $BiFeO_3/\alpha(\gamma)$-Fe_2O_3 ferromagnetic nano p/n junctions formed by dopant-induced phase separation. J Nanopart Res 15:1848

Rossell MD, Agrawal P, Borgschulte A, Hébert C, Passerone D, Ern R (2015) Direct evidence of surface reduction in monoclinic $BiVO_4$. Chem Mater 27:3593

Song XC, Li WT, Huang WZ, Zhou H, Yin HY, Zheng YF (2015) Enhanced photocatalytic activity of cadmium-doped Bi_2WO_6 nanoparticles under simulated solar light. J Nanopart Res 17:134

Su YG, Lang JY, Cao N, Wang TT, Zhu BL, Wang XJ (2015) Morphological reconstruction and photocatalytic enhancement of $NaTaO_3$ nanocrystals via Cu_2O loading. J Nanopart Res 17:63

Wang DF, Tang JW, Zou ZG, Ye JH (2005) Photophysical and photocatalytic properties of a new series of visible-light-driven photocatalysts $M_3V_2O_8$ (M = Mg, Ni, Zn). Chem Mater 17:5177

Weng BC, Xu FH, Xu JG (2014) Hierarchical structures constructed by BiOX (X = Cl, I) nanosheets on CNTs/carbon composite fibers for improved photocatalytic degradation of methyl orange. J Nanopart Res 16:2766

Witzke T, Zhen S, Seff K, Doering T, Nasdala L, Kolitsch U (2001) Ronneburgite, $K_2MnV_4O_{12}$, a new mineral from Ronneburg, Thuringia, Germany: description and crystal structure. Am Mineral 86:1081

Xiong JH, Wu WM, Liu YH, Shen LJ, Wu L (2015) Fabrication of hierarchical CdS nanosphere via one-pot process for photocatalytic water splitting. J Nanopart Res 17:55

Yao WF, Ye JH (2006) Photocatalytic properties of a novel layered photocatalys $CsLaSrNb_2NiO_9$. Catal Lett 110:139

Yin H, Tsuzuki T, Millington KR, Casey PS (2014) A comparative interlaboratory study on photocatalytic activity of commercial ZnO and CeO_2 nanoparticles. J Nanopart Res 16:2641

Zhang XH (2014) Synthesis of Ni doped $InVO_4$ for enhanced photocatalytic hydrogen evolution using glucose as electron donor. Catal Lett 144:1253

Zhang F, Song WJ, Zhao ZS, Cheng Y (2014a) Photo-catalytic properties of doped or substituted polyaniline-coated Fe_3O_4 nanoparticles. J Nanopart Res 16:2666

Zhang YY, Guo YP, Duan H, Li H, Sun CY, Liu HZ (2014b) Facile synthesis of V^{4+} self-doped, [010] oriented $BiVO_4$ nanorods with highly efficient visible light-induced photocatalytic activity. Phys Chem Chem Phys 16:24519

Zhang FF, Liu W, Liu YS, Wang JY, Ji GB (2015) Fabrication and enhanced photocatalytic properties of $Pt@SiO_2@TiO_2$ composites by surface plasma resonance from Pt nanoparticles. J Nanopart Res 17:62

Zhu HL, Chen DM, Yue D, Wang ZH, Ding H (2014) In-situ synthesis of g-C_3N_4-P25 TiO_2 composite with enhanced visible light photoactivity. J Nanopart Res 16:2632